



Three-dimensional sparse seismic deconvolution based on earth Q model

Deborah Pereg^{a,*}, Israel Cohen^a, Anthony A. Vassiliou^b

^a Technion – Israel Institute of Technology, Israel

^b GeoEnergy, Houston, TX, United States of America

ARTICLE INFO

Article history:

Received 1 April 2018

Revised 29 June 2018

Accepted 21 August 2018

Available online 23 August 2018

Keywords:

Seismic inversion

Seismic signal

Sparse reflectivity

Reflectivity estimation

Earth Q model

ABSTRACT

We propose a multichannel efficient method for recovery of three-dimensional (3D) reflectivity signal from 3D seismic data. The algorithm consists of solving convex constrained optimization problems that promote the sparsity of the solution. It is formulated so that it fits the earth Q model that describes the attenuation and dispersion propagation effects of reflected waves. At the same time, the method also takes into account the relations between spatially-neighboring traces. These three features together with low computational cost make the proposed method a reliable solution for the emerging need to accurately estimate reflectivity from large volumes of 3D seismic data. We also derive a theoretical bound on the recovery error in the case of horizontal layered sub-terrain. We show that the recovery error is inversely proportional to the number of traces taken into account in the estimation process. Synthetic and real data examples demonstrate the robustness of the proposed technique compared to single-channel recovery.

© 2018 Elsevier B.V. All rights reserved.

1. Introduction

Reflection seismology aims at estimating the properties of earth subsurface layers. The seismic data gives insight into the internal structure of the subsurface. It visualizes geological structures such as layers, traps and faults. To acquire the data, a source of energy is used to transmit a short duration acoustic pulse (the wavelet) into the ground. Then, reflected pulses are received by an array of geophones and further processed into 3D seismic data [1–3]. A 3D section of seismic data consists of two spatial dimensions referred to as in-line and cross line. The third dimension is the two-way time of arrival of reflections which corresponds to the reflector's depth in the ground. By in-line direction we refer to the direction parallel to the receiver lines, which is the direction in which the data was acquired. Cross-line direction is the orthogonal direction.

Similarly to other acoustic imaging methods (such as ultrasound [4]), the acoustic energy is reflected at discontinuities in the medium impedance and recorded by an array of geophones on the ground. Each seismic trace (a column in the seismic 3D data) is modeled as a weighted superposition of one-dimensional (1D) pulses degraded by additive noise. The resolution of the given data is limited since the pulse is band-limited and changes over time.

Our goals are to recover the earth structure (the reflectivity) hidden in the observed seismic data, to increase its resolution and to overcome loss of information due to noise and due to attenuation of the reflected waves as they travel through the acoustic medium. It is assumed that the seismic signal is essentially free of multiple reflections (multiples are events that have undergone more than one reflection [1]).

In previous works it is often the case that the seismic inversion problem is solved by simply breaking the data into independent vertical 1D deconvolution problems. Each reflectivity channel is recovered from the corresponding inline trace or cross line trace of a vertical cross section of the seismic data. The core assumption is that a reflectivity channel is a sparse spike train [2,5–12]. This approach enables the use of ℓ_1 minimization problem solving to find stable reflectivity solutions [7–11,13,14]. Similar methods, which decompose a signal into its building blocks (atoms) [15], are studied in many other applications in signal processing and machine learning, such as image processing [16] and compressed sensing [17]. For further details we refer the reader to [4,18–26].

Multichannel seismic deconvolution methods [27–36] promote horizontal continuity of the seismic reflectivity. These methods take into account more than one trace in each channel estimation. Heimer and Cohen [32] propose a method based on Markov-Bernoulli random-field (MBRF) modeling. They apply the Viterbi algorithm [37] to conduct a search of the most likely sequences of reflectors connected by legal transitions. Ram et al. [34] also

* Corresponding author.

E-mail address: deborahp@tx.technion.ac.il (D. Pereg).

propose two multichannel blind deconvolution algorithms for two-dimensional (2D) seismic data. Assuming a Markov-Bernoulli-Gaussian (MBG) reflectivity model, each reflectivity channel is estimated from the corresponding observed seismic trace, considering an estimate of the previous reflectivity channel or estimates of both the previous and subsequent channels.

Most inversion methods depend on a time-invariant model. Namely, the traveling wavelet is modeled as a 1D time-invariant signal in both horizontal and vertical directions. Despite the fact that the typical seismic wavelet is time-variant, time-depth variations in the waveform are often ignored. Seismic inverse Q-filtering [38–41] is a process targeted at inverting phase and amplitude distortions of the propagating and reflected acoustic waves. Ideally, the process of inverse Q filtering improves the resolution and increases the signal-to-noise ratio (SNR). However, it is often impractical and computationally costly.

Nonstationary deconvolution methods perform deconvolution of the seismic data that also compensates for waves attenuation. Among these methods are the Gabor deconvolution algorithm proposed by Margrave et al. [42], nonstationary sparse reflectivity inversion (NSRI) method suggested by Chai et al. [43], nonstationary deconvolution algorithm based on spectral modeling [44], and variable-step-sampling (VSS) hyperbolic smoothing developed by Li et al. [45].

Nowadays seismic techniques concentrate more on 3D data. Thus recovering a 3D reflectivity function that represents the earth's impulse response [1]. Application of 1D methods to 3D data is clearly suboptimal, yet, due to practical convenience many seismic algorithms are 1D trace-by-trace algorithms. In [36] Ghoalami and Sacchi introduce a fast 3D blind seismic deconvolution algorithm. The algorithm considers the seismic wave field as a 3D signal and alternates between two stages: 3D reflectivity estimation, which promotes temporal continuity, and source estimation.

In a previous work [46] we have shown that the recovery of the seismic reflectivity can be achieved efficiently based on earth Q model by solving a simple convex optimization problem. We derived theoretical bounds on the recovery error, and on the localization error. It is proved that recovered reflectors in the estimated reflectivity are in close proximity to reflectors in the true reflectivity signal.

This paper presents a novel robust method for recovery of 3D reflectivity signal from 3D seismic data. We show that the solution of a convex optimization problem, which takes into consideration a time-variant signal model, results in a stable recovery. The problem is formulated so that the relations between spatially close traces are also taken into account. The algorithm is applied to synthetic and real seismic data, demonstrating that the proposed algorithm restores reflectors amplitudes and locations with high precision. Our work may also be applicable to other imaging data, such as ultrasound imaging and radar.

The paper is organized as follows. In Section 2, we briefly review the seismic inversion problem formulation. In Section 3, we describe the 3D recovery method. Section 4 focuses on numerical experiments and real data results. Finally, in Section 5, we summarize and explore further research options.

2. Signal model

2.1. Reflectivity model

We assume an unknown 3D reflectivity signal. Each 1D channel (column) in the reflectivity is formulated as a superposition of point sources. In the discrete setting, assuming a sampling rate F_s , and that the set of delays $T = \{t_m\}$ lies on a grid k/F_s , $k \in \mathbb{Z}$, i.e.,

$t_m = k_m/F_s$, the reflectivity is given by

$$x[k] = \sum_m c_m \delta[k - k_m], \quad k \in \mathbb{Z}, \quad c_m \in \mathbb{R} \quad (1)$$

where $\delta[k]$ denotes the Kronecker delta function (see [47]), and $\sum_m |c_m| < \infty$. $K = \{k_m\}$ is the set of discrete delays corresponding to the spikes locations.

Each inline or crossline seismic discrete trace in the observed seismic 3D data is of the form

$$y[k] = \sum_n x[n] g_{\sigma,n}[k - n] + w[k], \quad n \in \mathbb{Z} \quad (2)$$

where $\{g_{\sigma,n}\}$ is a known set of kernels (pulses) corresponding to a possible set of time delays. $\sigma > 0$ is a known scaling parameter, and $w[k]$ is additive noise. In [46] we discuss specific requirements for $\{g_{\sigma,n}\}$. Our purpose is to reveal the true support $K = \{k_m\}$ and the spikes' amplitudes $\{c_m\}$ hidden in each of the seismic traces.

Note that the conventional convolution model assumes a time-invariant wavelet, meaning that all kernels are identical ($g_{\sigma,n}[k] = g_{\sigma}[k] \forall n$) [4,26]. Unfortunately, this assumption is often not satisfied. As in [46], we suggest to take into consideration a set of different kernels $\{g_{\sigma,n}\}$. Each pulse in the set is determined according to the time (depth) t_n it corresponds to, in accordance with the earth Q model [38,46,48,49].

In a previous work [46] we presented a 1D algorithm that recovers the seismic reflectivity based on earth Q model. We also presented theoretical bounds on the recovery error, and on the localization error. In this paper we expand these results to 3D setting. We propose a way to improve the results by taking advantage of the ability to assess the relation between a point in the data and adjacent points, using discontinuity measures [50,51]. This approach enables the use of multiple traces in the seismic data for the estimation of each channel to overcome noisy environments and highly attenuating media.

To this end, we recall interrelated fundamental properties reviewed in [46]. For further details we refer the reader to [4,23,26,46].

2.2. Earth Q model

Let us consider an initial source waveform $s(t)$ defined as the real-valued Ricker wavelet

$$s(t) = \left(1 - \frac{1}{2} \omega_0^2 t^2\right) \exp\left(-\frac{1}{4} \omega_0^2 t^2\right). \quad (3)$$

ω_0 is the most energetic (dominant) radial frequency [48]. Hence, in this setting, the scaling parameter is $\sigma = \omega_0^{-1}$. Following the earth Q-model [49], given Q - the medium quality factor [38] - a reflected wave at travel time t_n , is

$$u_n(t - t_n) = \text{Re} \left\{ \frac{1}{\pi} \int_0^\infty S(\omega) \exp[j(\omega t - \kappa r(\omega))] d\omega \right\}, \quad (4)$$

where $S(\omega)$ is the Fourier transform of the source waveform $s(t)$,

$$\kappa r(\omega) \triangleq \left(1 - \frac{j}{2Q}\right) \left|\frac{\omega}{\omega_0}\right|^{-\gamma} \omega t_n, \quad (5)$$

$$\gamma \triangleq \frac{2}{\pi} \tan^{-1} \left(\frac{1}{2Q}\right) \approx \frac{1}{\pi Q}, \quad (6)$$

Q was also defined by Kjartansson [38] as the portion of energy lost during each cycle or wavelength. In this manner, in the frequency domain, two exponential operators represent velocity dispersion (phase changes) and energy absorption (amplitude attenuation) of the traveling pulses

$$U_n(\omega) \exp^{-j\omega t_n} = S(\omega) \exp\left(-j \left|\frac{\omega}{\omega_0}\right|^{-\gamma} \omega t_n\right) \exp\left(-\left|\frac{\omega}{\omega_0}\right|^{-\gamma} \frac{\omega t_n}{2Q}\right). \quad (7)$$

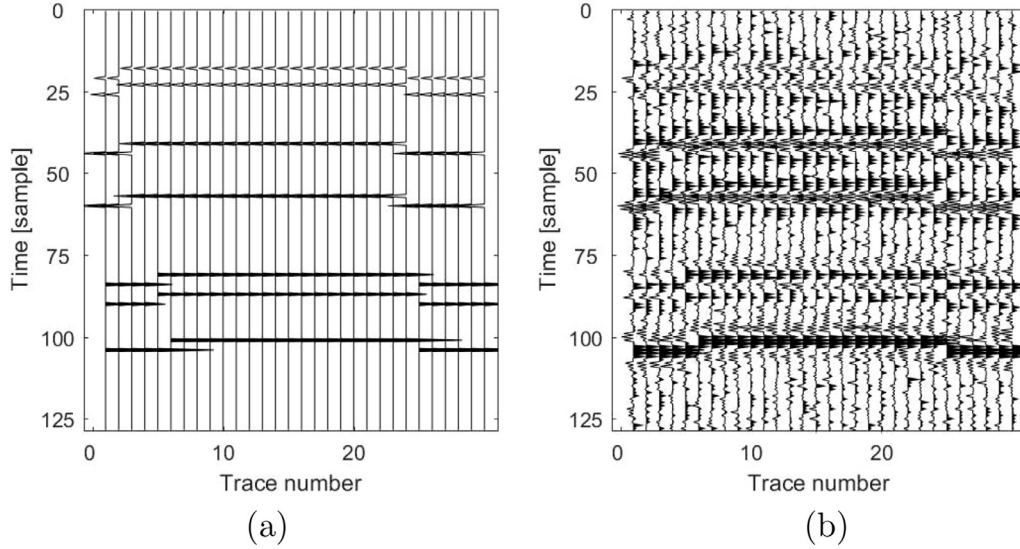


Fig. 1. Synthetic reflectivity and seismic data: (a) Synthetic 2D reflectivity section; (b) 2D seismic data (SNR = 5 dB).

Hence, the time-domain seismic pulse reflected at two-way travel time (depth) t_n is

$$u_n(t - t_n) = \frac{1}{2\pi} \int U_n(\omega) \exp[j\omega(t - t_n)] d\omega. \quad (8)$$

Q is assumed to be known. Consequently, the known set of kernels (pulses) $\{g_{\sigma, n}\}$ is defined as

$$g_{\sigma, n}(t - t_n) = u(t - t_n)|_{\sigma=\omega_0^{-1}}. \quad (9)$$

3. Seismic 3D recovery

It is shown in [46] that single-channel recovery of the seismic reflectivity could be performed by solving the optimization problem

$$\min_{\hat{x} \in \ell_1(\mathbb{Z})} \|\hat{x}\|_1 \quad \text{subject to} \quad \|y[k] - \sum_n \hat{x}[n]g_{\sigma, n}[k - n]\|_1 \leq d, \quad (10)$$

where $\|\hat{x}\|_1 = \sum_k |\hat{x}[k]|$.

To this end, we consider 3D seismic data and develop a 3D recovery method based on convex optimization. We do not assume horizontal continuous layers or any other specific geological structure.

Assume an inline or a crossline seismic trace $\mathbf{y}_{i, j}$ and $N - 1$ spatially neighboring traces $\{\mathbf{y}_{i+u, j+v}\}$, where $(u, v) \in \Gamma$ such that $\Gamma \subseteq \{(u, v) \in \mathbb{Z}^2, (u, v) \neq (0, 0)\}$ and $|\Gamma| = N - 1$. Denote some local discontinuity measure as a column vector $\mathbf{a}_{i, j}$. Each element $a_{i, j}[k]$ is associated with a distinguished point in some analysis cube, generically represented here by (i, j, k) . We choose a measure such that $0 \leq a_{i, j}[k] \leq 1$. For maximum discontinuity $a_{i, j}[k] = 0$, whereas for minimum discontinuity $a_{i, j}[k] = 1$. The value $a_{i, j}[k]$ describes the likelihood that a given point lies on a fault surface. In a sense, each element in $\mathbf{a}_{i, j}$ is a measure of the resemblance of the corresponding element in $\mathbf{y}_{i, j}$ to points in neighboring traces $\{\mathbf{y}_{i+u, j+v}\}$.

Assume G is an operator matrix such that $(G)_{k, n} = g_{\sigma, n}[k - n]$. Then, we can write

$$\mathbf{y}_{i, j} = G\mathbf{x}_{i, j} + \mathbf{w}_{i, j}, \quad (11)$$

where $\mathbf{x}_{i, j}$ is the corresponding reflectivity column and $\mathbf{w}_{i, j}$ is additive noise.

Then, the estimated reflectivity column $\hat{\mathbf{x}}_{i, j}$ is the solution of the optimization problem

$$\min \|\hat{\mathbf{x}}_{i, j}\|_1 \quad \text{subject to} \quad f(\hat{\mathbf{x}}_{i, j}) \leq \Delta, \quad (12)$$

where

$$f(\hat{\mathbf{x}}_{i, j}) = \|\mathbf{y}_{i, j} - G\hat{\mathbf{x}}_{i, j}\|_2 + \sum_{(u, v) \in \Gamma} \|A_{i, j}A_{i+u, j+v}(\mathbf{y}_{i+u, j+v} - G\hat{\mathbf{x}}_{i, j})\|_2, \quad (13)$$

where $A_{i, j} = \text{diag}(\mathbf{a}_{i, j})$, and $A_{i+u, j+v} = \text{diag}(\mathbf{a}_{i+u, j+v})$. Since $A_{i, j}$ and $A_{i+u, j+v}$ describe the similarity between one spike (or null) location to close locations in a small volume, multiplying the residual error of neighboring traces by $A_{i, j}A_{i+u, j+v}$ enables the use of the available information about a group of channels, for the estimation of the true reflectivity value in each location in the volume. Wherever there is discontinuity in the volume, there is no dependency between one pixel to another in the defined volume, and then the estimation of this specific point will not rely on other close points. This process helps us overcome noise artifacts and attenuation, rather than always assume similarity between points with a certain distance, as in [52].

We assume noise signals with bounded mean energy

$$E\|\mathbf{w}_{i, j}\|_2^2 = E\|\mathbf{y}_{i, j} - G\mathbf{x}_{i, j}\|_2^2 \leq S_w^2 \quad \forall i, j$$

where $\|\mathbf{w}\|_2 \triangleq \sqrt{\sum_k w^2[k]}$, and E denotes mathematical expectation. Since the noise signals are uncorrelated by assumption, we can choose

$$\Delta = NS_w$$

A brief review of two suitable discontinuity measures and their use in implementing the above method can be found in Appendix C.

3.1. Recovery-error bound for horizontal layers

Theorem 1. Assume N seismic traces that correspond to N identical reflectivity channels. Namely,

$$y_i[k] = \sum_n x[n]g_{\sigma, n}[k - n] + w_i[k], \quad E\|w_i\|_2^2 \leq S_w^2, \quad i = 1, 2, \dots, N,$$

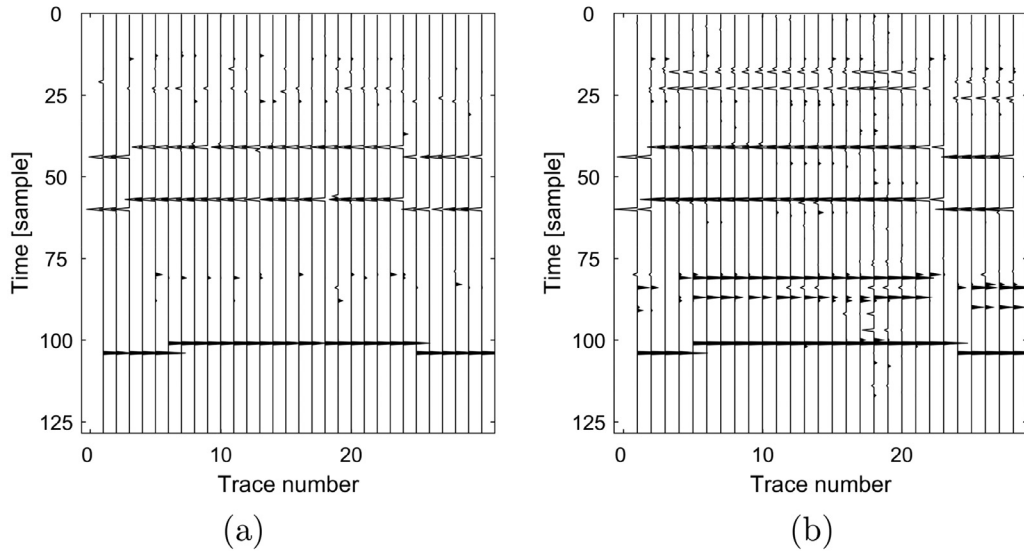


Fig. 2. Synthetic 2D recovery results: (a) Single-channel; (b) Multichannel.

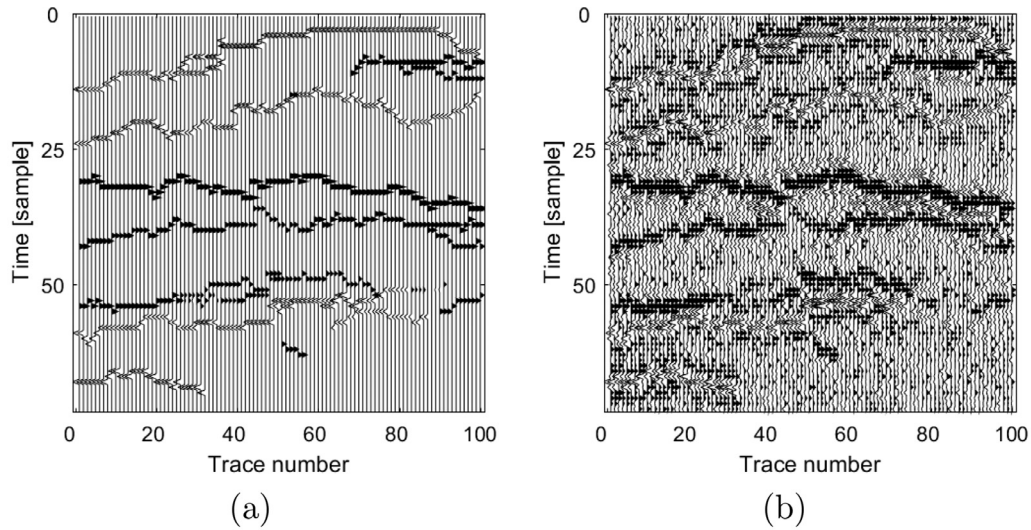


Fig. 3. Synthetic reflectivity and seismic data: (a) Synthetic 2D reflectivity section; (b) 2D seismic data (SNR = 5 dB).

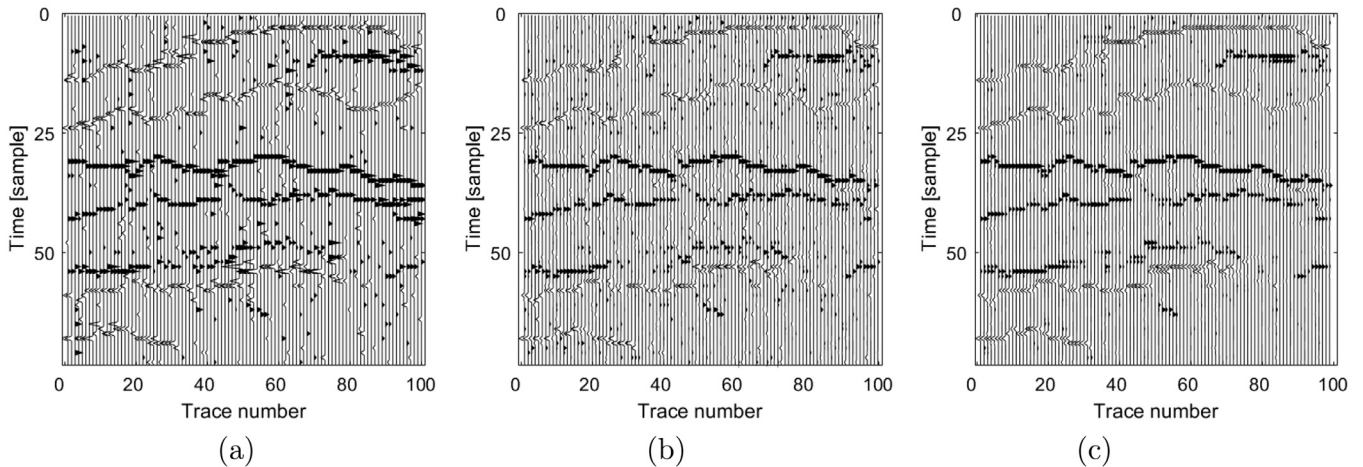


Fig. 4. Synthetic 2D recovery results: (a) MC-II, $\rho = 0.74$; (b) Single-channel, $\rho = 0.85$; (c) Multichannel, $\rho = 0.9$.

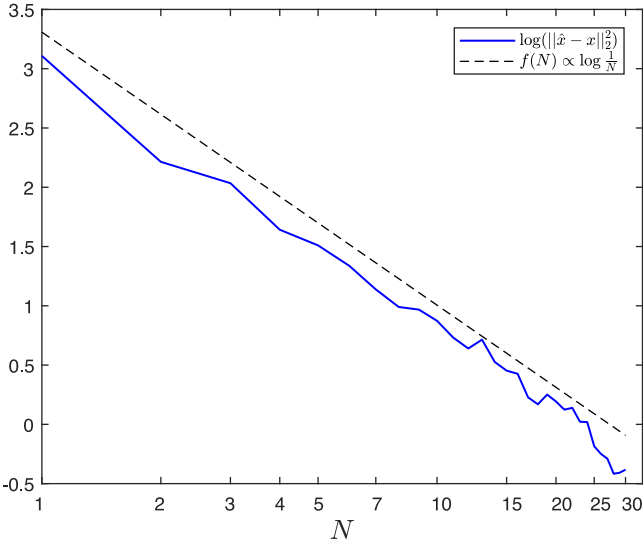


Fig. 5. Recovery error $\log(\|\hat{\mathbf{x}} - \mathbf{x}\|_2^2)$ as a function of number of traces N for $Q = 500$.

(14)

where $\{g_{\sigma, n}\}$ is a set of admissible kernels sharing two common parameters $\varepsilon, \beta > 0$ (see [46, Definition 2.1], Appendix B). The parameters ε and β measure the concavity of a pulse near its midpoint. In other words, the set $\{y_i\}_{i=1}^N$ consists of N smeared versions of N identical reflectivity columns, corrupted by N different noise realizations. We assume the support K is sufficiently separated, meaning that it obeys the minimal separation condition (see [46, Definition 2.2], Appendix B), with a separation constant ν . Then, for

$F_s > 0$, the solution $\hat{\mathbf{x}}$ of

$$\begin{aligned} \min \quad & \|\hat{\mathbf{x}}\|_1 \\ \text{subject to} \quad & \sum_{i=1}^N \|\mathbf{y}_i - G\hat{\mathbf{x}}\|_2 \leq NS_w, \end{aligned} \quad (15)$$

satisfies

$$E\|\hat{\mathbf{x}} - \mathbf{x}\|_2^2 \leq \frac{64L_r\rho^2 S_w^2}{\beta^2\gamma_0^2 N}. \quad (16)$$

where L_r is the length of the estimated signal,

$$\rho \triangleq \max \left\{ \frac{\gamma_0}{\varepsilon^2}, (F_s\sigma)^2\alpha_0 \right\}$$

$$\alpha_0 = \max_n g_{\sigma, n}(0), \quad \gamma_0 = \min_n g_{\sigma, n}(0).$$

Proof. see Appendix A. \square

This bound ensures that in the case of perfectly horizontal layers, given N traces, under the separation condition, a signal of the form (2), can be recovered by solving the optimization problem formulated in (15). Furthermore, it guarantees that the mean squared error of the recovery is bounded. The error depends on the noise level and on the attenuation of the reflected waves. Most importantly the theoretical bound, affirmed by experimental results, demonstrates that given N realizations of the same reflectivity channel (as we have for horizontal reflectors), we can reduce noise power at least by a factor of N . In the noise-free case where $S_w = 0$, whether the spikes amplitudes are small or large, the restoration of the reflectivity is exact.

When $\gamma_0 = \alpha_0$ (time-invariant case)

$$E\|\hat{\mathbf{x}} - \mathbf{x}\|_2^2 \leq 64 \frac{L_r}{\beta^2} \max \left\{ \frac{1}{\varepsilon^4}, (F_s\sigma)^4 \right\} \frac{S_w^2}{N}.$$

The recovery error is proportional to the noise power. Flat kernels (small values of β) tend to result in larger errors. The SNR is increased by a factor that is equal to the number of traces.

In the time-variant setting most cases comply with $\frac{\gamma_0}{\varepsilon^2} < (F_s\sigma)^2\alpha_0$.

Then, the recovery error is bounded by

$$E\|\hat{\mathbf{x}} - \mathbf{x}\|_2^2 \leq 64 \frac{L_r (F_s\sigma)^4}{\beta^2} \left(\frac{\alpha_0}{\gamma_0} \right)^2 \frac{S_w^2}{N}.$$

Similarly to the time-invariant case, the error is linear with respect to the noise level S_w^2 . Moreover, since we know that small Q values correspond to higher $\frac{\alpha_0}{\gamma_0}$ ratios and smaller β values, the bound verifies that the error increases as Q gets smaller. In addition, since β measures the flatness of the kernel near the origin, we can see that flat kernels result in more false detections. In all cases, the error is inversely proportional to the number of channels, N .

4. Experimental results

In this section, we use synthetic and real data examples to demonstrate the performance of the proposed technique. We used CVX [53], to solve the ℓ_1 minimization in (10) and (12).

4.1. Synthetic data

We constructed a synthetic data set, simulating 2D reflectivity with two apparent faults. The reflectivity consists of 30 traces, each of 128 samples, with sampling interval of $T_s = 4$ ms. The reflectivity is depicted in Fig. 1(a). We created the seismic data as described in (2) using the Q model, with $Q=200$. The initial wavelet was a Ricker wavelet with $\omega_0 = 50\pi$, i.e., 25 Hz. To further degrade the signal and evaluate the recovery in noisy environment we added white Gaussian noise. The SNR is 5 dB. The seismic data is shown in Fig. 1(b).

The estimated reflectivities, obtained by single-channel and by the proposed multichannel recovery method are shown in Figs. 2(a) and (b), respectively. To implement the single-channel recovery we estimate all possible kernels as described above and solve (10). In this example, for the multichannel recovery we set $N = 3$, i.e., the optimization is performed by considering each seismic trace and both the preceding and subsequent traces. As a measure of discontinuity we use a binary version of the Local Structural Entropy (LSE) (see [50], Appendix C) using a threshold of $\tau = 0.02$. The correlation coefficient, between the original reflectivity and the estimated reflectivity, achieved by single-channel deconvolution is $\rho = 0.86$. Whereas, the correlation coefficient with our method, is $\rho = 0.95$. Visually comparing the results, it can be seen that the multichannel solution is much more accurate. The single-channel solution fails to recover parts of the layer boundaries and tends to annihilate weak spikes.

Another synthetic example is presented in Figs. 3 and 4. We generated a synthetic reflectivity of size 76×100 with an apparent fault (see Fig. 3(a)). Sampling interval is $T_s = 4$ ms. We create the seismic data depicted in Fig. 3(b), using $Q = \infty$ (no attenuation) and an initial Ricker wavelet with $\omega_0 = 80\pi$. We compare our results for $N = 2$ to the single channel deconvolution (Eq. 10) and to the multichannel time-invariant deconvolution algorithm described in [34] (MC-II). The estimated reflectivity sections, for the seismic data with SNR of 5 dB, are shown in Fig. 4(a)–(c). The multichannel method was implemented using the LSE measure. For this example, the correlation coefficient between the original reflectivity and the estimated reflectivity, with our method, are $\rho = 0.9$. Whereas the correlation coefficient achieved by single-channel deconvolution is $\rho = 0.85$, and $\rho = 0.74$ for MC-II.

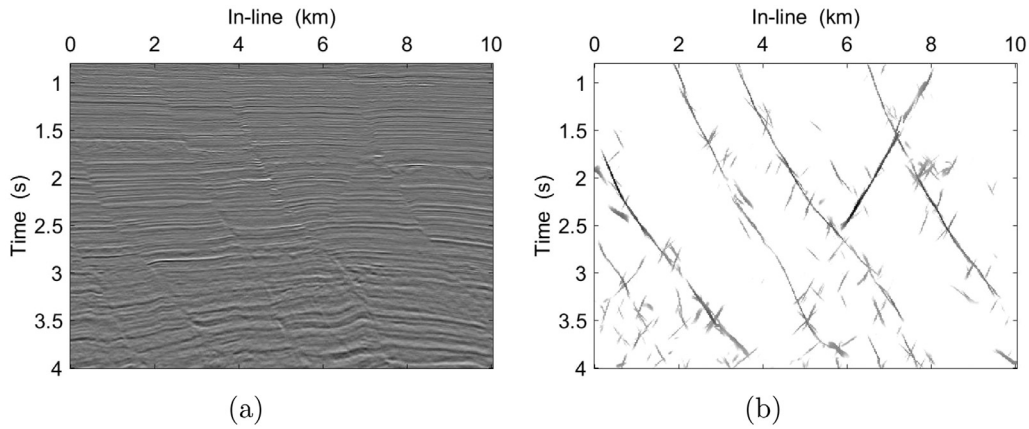


Fig. 6. Vertical cross-section at $y = 1.3$ km through: (a) seismic data (b) skeletonized LFE volume.

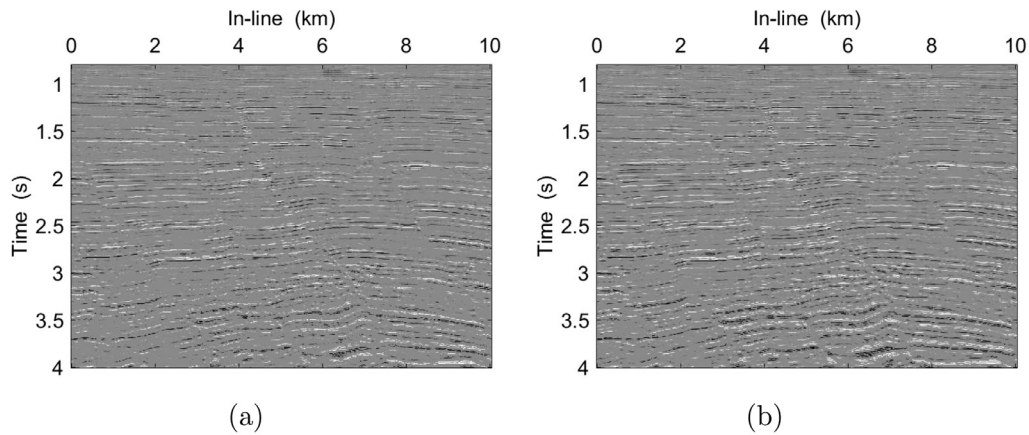


Fig. 7. Real data inversion results: (a) Estimated reflectivity - single-channel (c) Estimated reflectivity - multichannel.

The implementation of the above method entails low computational complexity. Solving the ℓ_1 minimization in (14) using CVX [53], the processing time of the seismic data set in Fig. 3(b), of size 102×100 , on Intel(R)Core(TM)i7-7820HQ@2.90 GHz is 32.0 s (average of 320 ms per trace). The processing time for the single-channel implementation is 35.4 s, and 60.0 s for MC-II. Generally speaking, the average processing time of the single-channel and multichannel implementation is approximately the same. The algorithm is fast and therefore applicable to large volumes of data.

To confirm the bound we deduced in Section 3.1, we examined the recovery error $\|\hat{x} - x\|_2^2$ as a function of the noise level S_w^2 and as a function of the number of traces N for different horizontal reflectivity realizations. Fig. 5 presents one example of the recovery error $\|\hat{x} - x\|_2^2$ as a function of the number of traces $1 \leq N \leq 30$ for $Q = 500$ and $\text{SNR} = 5$ dB, $T_s = 4$ ms and $L_r = 176$. As in Fig. 1, the reflectivity is modeled as a zero-mean Bernoulli-Gaussian process. The minimum distance between two spikes satisfies the minimal separation condition. The initial wavelet was a Ricker wavelet with $\omega_0 = 100\pi$, i.e., 50 Hz. As can be seen in Fig. 5 the error is inversely proportional to the number of traces, according to what we derived in Theorem 1.

4.2. Real data

We applied the proposed method, to real seismic data from a small land 3D survey (courtesy of GeoEnergy Inc., TX). The time interval is 4 ms; inline and cross line trace spacing is 25 m. A small subvolume with inline and crossline distances of 10 km (401×401 traces) is used for demonstration. Each trace is 4 s in duration

(1001 samples). Fig. 6(a) shows a vertical cross section through the seismic data. As a measure of discontinuity we used the skeletonized local-fault-extraction (LFE) presented in [51]. The seismic data through the LFE is presented in Fig. 6(b). We can assume the given seismic data is noise-free.

Assuming an initial Ricker wavelet with $\omega_0 = 50\pi$ (25 Hz), we estimated $Q = 200$ as described in [54]. Then, as a single-channel solution, we solved (15) for $N = 1$. A cross-section of the recovered reflectivity section by single-channel method is shown in Fig. 7(a). The seismic data reconstructed from the estimated reflectivity using the known sequence $\{g_{\sigma, n}(t)\}$, is shown in Fig. 8(a). Using the skeletonized LFE measure we computed the recovered reflectivity and its reconstructed seismic data. Fig. 7(b) shows the recovered reflectivity cross-section of a 3-channel implementation (i.e., $N = 3$). Each reflectivity column is recovered by taking into consideration its resemblance to two neighboring traces - one in the same vertical cross section and one in the adjacent cross-section. Fig. 9 shows a zoom into the reflectivity sections in offset range 2–10 km and time range 2.5–4 s.

The algorithm could be implemented for any number of neighboring traces. The user can determine the number of traces taken into account by the type of geological features that is of interest to the interpreter, and the required resolution. The sensitivity to noise and to small-scale discontinuities increases as the number of neighboring traces taken into consideration is smaller.

Visually examining these reflectivity sections, it can be seen that the layer boundaries in the estimates are distinct. Both structural features (such as faults) and stratigraphic features (such as channels) can be observed in the images. Also, the reconstructed

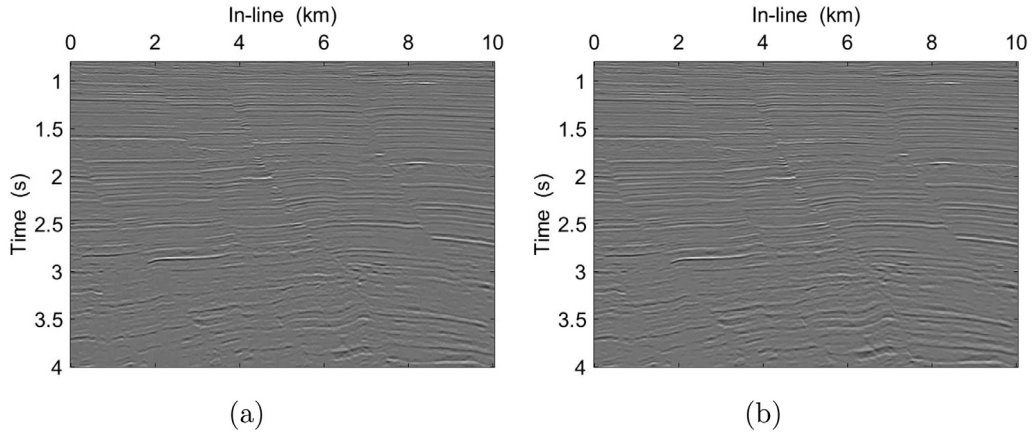


Fig. 8. Reconstructed seismic data: (a) Single-channel, $\rho_{y,\hat{y}} = 0.88$ (b) Multichannel, $\rho_{y,\hat{y}} = 0.90$.

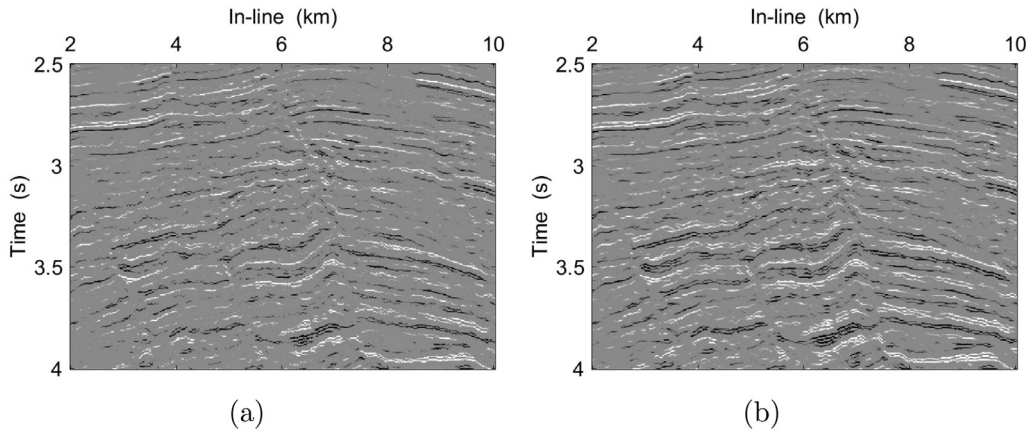


Fig. 9. A zoom into Fig. 8: (a) Estimated reflectivity - single-channel (c) Estimated reflectivity - multichannel.

seismic data seems to fit to the original given observation. Since the ground truth is unknown, we measure the accuracy in the location and amplitude of the recovered reflectivity spikes by the correlation coefficient between the reconstructed data to the given seismic data. A trace in the reconstructed data is $\hat{y} = G\hat{x}$, where \hat{x} is the estimated reflectivity. The correlation is calculated with respect to the noise-free seismic data. In this example we have $\rho_{y,\hat{y}} = 0.90$ for the multichannel result, which indicates that the reflectivity is estimated with high precision. For single-channel recovery we have $\rho_{y,\hat{y}} = 0.88$. Looking closely at the estimated reflectivities the differences are visible, despite only a few percent gain in correlation. The multichannel results look more continuous and more detailed, especially in deeper areas and near faults. In addition, some curves collapse into one curve in the single-channel estimated reflectivity and separate into two adjacent curves (layers) in the multichannel estimation.

5. Conclusions

Acquired 3D seismic data requires development of 3D processing algorithms. The recovery of 3D reflectivity is essential to the visualization of subterranean features. In recent years, there has been progress in the estimation of the reflectivity and the source wavelet function. Yet, existing methods have limited precision and are highly complex.

We have presented a 3D adaptive seismic recovery algorithm based on a time-variant model. The algorithm promotes sparsity of the solution. It also considers the attenuation and dispersion effects resulting in shape distortion of the wavelet. Furthermore,

the recovery takes into account the relations between consecutive traces in the 3D volume. These properties are all expressed in a simple convex optimization problem, making the algorithm suitable for large volumes of data. We have introduced practical results with synthetic and real data in highly attenuating noisy environment.

Future research can adapt the algorithm to other applications such as medical imaging. In exploration seismology the algorithm can also be modified to non-constant Q layers model. In addition, other discontinuity measures and sets of kernels could be investigated.

Acknowledgment

The authors thank the associate editor and the anonymous reviewers for their constructive comments and useful suggestions.

Appendix A

Proof of Theorem 1. Denote $g_m(t) \triangleq g_{\sigma,m}(t)|_{\sigma=1}$. In [46], we showed that there exists a function of the form

$$q(t) = \sum_m a_m g_m(t - t_m) + b_m g_m^{(1)}(t - t_m),$$

that satisfies

$$\begin{aligned} |q(t_k)| &= 1 \quad \forall t_k \in T, \\ q^{(1)}(t_k) &= 0 \quad \forall t_k \in T, \end{aligned}$$

where $T \triangleq \{t_m\}$ is a set of delays obeying the separation condition (see [46, Definition 2.2], Appendix B). Notice that $q(t)$ is built such that $\langle q, x \rangle \triangleq \int q(t)x(t)dt = \sum_m |c_m|$. Also, $|q(t)|$ reaches a local maximum on the true support. This way, we can decouple the estimation error on the true support of the reflectivity $\{t_m\}$, from the amplitude of the rest of the estimated spikes.

To prove Theorem 1 we recall the following proposition and two lemmas (see [46, Appendix A] for a rigorous proof).

Proposition 2. Assume a set of delays $T \triangleq \{t_m\}$ that satisfies the separation condition (see [46, Definition 2.2], Appendix B), and let $\{g_m\}$ be a set of admissible kernels (see [46, Definition 2.1], Appendix B). Then, there exist coefficients $\{a_m\}$ and $\{b_m\}$ such that

$$q(t) = \sum_m a_m g_m(t - t_m) + b_m g_m^{(1)}(t - t_m), \quad (17)$$

$$|q(t_k)| = 1 \quad \forall t_k \in T, \quad (18)$$

and

$$q^{(1)}(t_k) = 0 \quad \forall t_k \in T. \quad (19)$$

The coefficients are bounded by

$$\|\mathbf{a}\|_\infty \leq \frac{3\nu^2}{3\gamma_0\nu^2 - 2\pi^2\tilde{C}_0}, \quad (20)$$

$$\|\mathbf{b}\|_\infty \leq \frac{3\pi^2\tilde{C}_1\nu^2}{(3\gamma_2\nu^2 - \pi^2\tilde{C}_2)(3\gamma_0\nu^2 - 2\pi^2\tilde{C}_0)}, \quad (21)$$

where $\mathbf{a} \triangleq \{a_m\}$, $\mathbf{b} \triangleq \{b_m\}$ are coefficient vectors and

$$\tilde{C}_l = \max_m C_{l,m}, \quad l = 0, 1, 2, 3.$$

We also have

$$a_m \geq \frac{1}{\alpha_0 + 2\tilde{C}_0P(\nu) + \frac{(2\tilde{C}_1P(\nu))^2}{\gamma_2 - 2\tilde{C}_2P(\nu)}}, \quad (22)$$

where $P(\nu) \triangleq \frac{\pi^2}{6\nu^2}$.

Lemma 3. Under the separation condition with $\varepsilon < \nu/2$, $q(t)$ as in Proposition 2 satisfies $|q(t)| < 1$ for $t \notin T$.

Now, assume \hat{x} is the solution of the optimization problem in (12). We assume Δ is large enough so that the solution \hat{x} obeys $\|\hat{x}\|_1 \leq \|x\|_1$. Denote the error $h[k] \triangleq \hat{x}[k] - x[k]$. We separate $h[k]$ into $h[k] = h_K[k] + h_{K^c}[k]$, where $h_K[k]$'s support is in the true support $K \triangleq \{k_m\}$. If $h_K[k] = 0 \forall k$, then $h[k] = 0 \forall k$, because if $h_K[k] = 0 \forall k$ and $h[k] \neq 0$ for some k , it would mean that $h_{K^c}[k] \neq 0$ for some k , and therefore $\|\hat{x}\|_1 > \|x\|_1$.

Under the separation condition, the set $T = \{t_m\}$ satisfies $t_i - t_j \geq \nu\sigma$ for $i \neq j$. We know that according to Proposition 2 [46, Proposition 3] there exists $q(t)$ of the form (17) such that

$$q(t_m) = q\left(\frac{k_m}{F_s}\right) = \text{sgn}(h_K[k_m]) \quad \forall k_m \in K. \quad (23)$$

In addition, $q(t)$ also obeys $|q(t)| < 1$ for $t \notin T$.

We then define

$$q_\sigma(t) = q\left(\frac{t}{\sigma}\right) = \sum_m a_m g_{m,\sigma}\left(t - \frac{k_m}{F_s}\right) + b_m g_{m,\sigma}^{(1)}\left(t - \frac{k_m}{F_s}\right).$$

So that

$$q_\sigma[k_m] \triangleq q_\sigma\left(\frac{k_m}{F_s}\right) = \text{sgn}(h_K[k_m]) \quad \forall k_m \in K,$$

and

$$|q_\sigma[k]| < 1 \quad \forall k \notin K.$$

Denote $g_{m,\sigma}^{(1)}[k] \triangleq g_{m,\sigma}^{(1)}\left(\frac{k}{F_s}\right)$. We can observe that

$$\begin{aligned} E \left\| q_\sigma[k] h[k] \right\|_2 &= E \left\| \left(\sum_{k_m \in K} a_m g_{m,\sigma}[k - k_m] + b_m g_{m,\sigma}^{(1)}[k - k_m] \right) h[k] \right\|_2 \\ &\leq \|a\|_\infty E \left\| \sum_m g_{m,\sigma}[k - k_m] h[k] \right\|_2 + \|b\|_\infty E \left\| \sum_m g_{m,\sigma}^{(1)}[k - k_m] h[k] \right\|_2, \end{aligned} \quad (24)$$

where we have used the Cauchy–Schwartz inequality. We can also infer that,

$$\begin{aligned} E \left\| \sum_m g_{m,\sigma}[k - k_m] h[k] \right\|_2 &= E \left\| \sum_m g_{m,\sigma}[k - k_m] \hat{x}[k] - \sum_m g_{m,\sigma}[k - k_m] x[k] \right\|_2 \\ &= E \left\| G\hat{\mathbf{x}} - G\mathbf{x} \right\|_2 \\ &= E \left\| \frac{1}{N} \sum_{i=1}^N \mathbf{y}_i - G\mathbf{x} - \left(\frac{1}{N} \sum_{i=1}^N \mathbf{y}_i - G\hat{\mathbf{x}} \right) \right\|_2 \\ &\leq E \left\| \frac{1}{N} \sum_{i=1}^N \mathbf{y}_i - G\mathbf{x} \right\|_2 + E \left\| \frac{1}{N} \sum_{i=1}^N \mathbf{y}_i - G\hat{\mathbf{x}} \right\|_2 \\ &\leq \frac{2S_w}{\sqrt{N}}, \end{aligned}$$

where we have used

$$E \left\| \frac{1}{N} \sum_{i=1}^N \mathbf{y}_i - G\mathbf{x} \right\|_2 \leq \frac{S_w}{\sqrt{N}},$$

because the noise signals are uncorrelated and have bounded mean ℓ_2 norm

$$E \|\mathbf{w}_i\|_2 = E \|\mathbf{y}_i - G\mathbf{x}\|_2 \leq S_w.$$

We also used,

$$\left\| \frac{1}{N} \sum_{i=1}^N \mathbf{y}_i - G\hat{\mathbf{x}} \right\|_2 \leq \frac{S_w}{\sqrt{N}},$$

which is inferred from the constraint on the solution. An estimated reflectivity channel obeys (15). Accordingly,

$$\sum_{i=1}^N \|\mathbf{y}_i - G\hat{\mathbf{x}}\|_2^2 \leq NS_w^2.$$

It follows that,

$$\begin{aligned} \sum_{i=1}^N \|\mathbf{G}\mathbf{x} - G\hat{\mathbf{x}} + \mathbf{w}_i\|_2^2 &\leq N \|\mathbf{w}_i\|_2^2 \\ N \|\mathbf{G}\mathbf{x} - G\hat{\mathbf{x}}\|_2^2 + 2 \sum_{i=1}^N \langle \mathbf{w}_i, \mathbf{G}\mathbf{x} - G\hat{\mathbf{x}} \rangle &+ \sum_{i=1}^N \|\mathbf{w}_i\|_2^2 \leq N \|\mathbf{w}_i\|_2^2 \\ \|\mathbf{G}\mathbf{x} - G\hat{\mathbf{x}}\|_2^2 + \frac{2}{N} \sum_{i=1}^N \langle \mathbf{w}_i, \mathbf{G}\mathbf{x} - G\hat{\mathbf{x}} \rangle &\leq 0 \\ \|\mathbf{G}\mathbf{x} - G\hat{\mathbf{x}}\|_2^2 + 2 \langle \frac{1}{N} \sum_{i=1}^N \mathbf{w}_i, \mathbf{G}\mathbf{x} - G\hat{\mathbf{x}} \rangle &+ \left\| \frac{1}{N} \sum_{i=1}^N \mathbf{w}_i \right\|_2^2 \leq \left\| \frac{1}{N} \sum_{i=1}^N \mathbf{w}_i \right\|_2^2 \\ \|\mathbf{G}\mathbf{x} - G\hat{\mathbf{x}} + \frac{1}{N} \sum_{i=1}^N \mathbf{w}_i\|_2^2 &\leq \frac{S_w^2}{N}, \end{aligned}$$

which means that,

$$\left\| \frac{1}{N} \sum_{i=1}^N \mathbf{y}_i - \mathbf{G}\hat{\mathbf{x}} \right\|_2^2 \leq \frac{S_w^2}{N}.$$

The estimated trace $\mathbf{G}\hat{\mathbf{x}}$, reconstructed from the solution $\hat{\mathbf{x}}$, is as close to the averaged trace as the true noise-free signal $\mathbf{G}\mathbf{x}$. The set of reflected pulses $\{g_m\}$ is a set of admissible kernels. Therefore,

$$|g_{m,\sigma}^{(1)}[k - k_m]| = \left| g_m^{(1)} \left(\frac{k - k_m}{F_s \sigma} \right) \right| \leq \frac{C_{1,m}}{1 + \left(\frac{k - k_m}{F_s \sigma} \right)^2}. \quad (25)$$

In addition, under the separation condition we have $|k_i - k_j| \geq F_s \nu \sigma \quad \forall k_i, k_j \in K$. It follows that, for any k

$$\sum_{k_m \in K} \left(\frac{1}{1 + \left(\frac{k - k_m}{F_s \sigma} \right)^2} \right)^2 < 4(1 + P(\nu))^2, \quad (26)$$

where

$$\sum_{n=1}^{\infty} \frac{1}{1 + (n\nu)^2} \leq P(\nu) \triangleq \frac{\pi^2}{6\nu^2}.$$

Consequently,

$$E \left\| \sum_m g_{m,\sigma}^{(1)}[k - k_m] h[k] \right\|_2^2 \leq \tilde{C}_1^2 \sum_{k \in \mathbb{Z}} E |h[k]|^2$$

$$\sum_{k_m \in K} \frac{1}{\left(1 + \left(\frac{k - k_m}{N\sigma} \right)^2 \right)^2} < 4\tilde{C}_1^2 (1 + P(\nu))^2 E \|h\|_2^2.$$

So we have,

$$E \left\| q_\sigma[k] h[k] \right\|_2 \leq \frac{2S_w}{\sqrt{N}} \|a\|_\infty + 2\tilde{C}_1 (1 + P(\nu)) \|b\|_\infty E \|h\|_2. \quad (27)$$

On the other hand,

$$E \left\| q_\sigma[k] h[k] \right\|_2 = E \left\| q_\sigma[k] (h_K[k] + h_{K^c}[k]) \right\|_2$$

$$\geq E \left\| q_\sigma[k] h_K[k] \right\|_2 - E \left\| q_\sigma[k] h_{K^c}[k] \right\|_2$$

$$\geq E \|h_K[k]\|_2 - \max_{k \in \mathbb{Z} \setminus K} |q_\sigma[k]| E \|h_{K^c}[k]\|_2, \quad (28)$$

where we have used that the absolute value of $q_\sigma[k]$ in the support is one. Combining (27) and (28) we get,

$$E \|h_K\|_2 - \max_{k \in \mathbb{Z} \setminus K} |q_\sigma[k]| E \|h_{K^c}\|_2 \leq \frac{2S_w}{\sqrt{N}} \|a\|_\infty$$

$$+ 2\tilde{C}_1 (1 + P(\nu)) \|b\|_\infty E \|h\|_2. \quad (29)$$

In the proof of Lemma 3 [46] we have shown that for $|k - k_m| \leq \varepsilon F_s \sigma$, for some $k_m \in K$

$$|q_\sigma[k]| = \left| q_\sigma \left(\frac{k}{F_s \sigma} \right) \right| \leq 1 - \frac{\beta}{2\alpha_0 (F_s \sigma)^2}.$$

We have also shown in [46] that for $|k - k_m| > \varepsilon F_s \sigma$ for all $k_m \in K$

$$|q_\sigma[k]| = \left| q \left(\frac{k}{F_s \sigma} \right) \right| \leq 1 - \frac{\beta \varepsilon^2}{2\gamma_0}.$$

To sum up

$$\max_{k \in \mathbb{Z} \setminus K} |q_\sigma[k]| \leq 1 - \frac{\beta}{2\rho} \quad (30)$$

where $\rho \triangleq \max \left\{ \frac{\gamma_0}{\varepsilon^2}, (F_s \sigma)^2 \alpha_0 \right\}$. Now, Substituting (30) into (29) we get,

$$E \|h_K\|_2 - \left(1 - \frac{\beta}{2\rho} \right) E \|h_{K^c}\|_2 \leq \frac{2S_w}{\sqrt{N}} \|a\|_\infty$$

$$+ 2\tilde{C}_1 (1 + P(\nu)) \|b\|_\infty E \|h\|_2. \quad (31)$$

We know from (12) that

$$\|x\|_1 \geq \|\hat{x}\|_1 = \|x + h\|_1 = \|x + h_K\|_1 + \|h_{K^c}\|_1$$

$$\geq \|x\|_1 - \|h_K\|_1 + \|h_{K^c}\|_1,$$

which leads us to

$$\|h_K\|_1 \geq \|h_{K^c}\|_1.$$

It is known that

$$\|h\|_2 \leq \|h\|_1 \leq \sqrt{L_r} \|h\|_2,$$

where L_r is the length of the estimated signal. Combining this with (31) leads us to

$$E \|h\|_2 \leq E \|h\|_1 = E \|h_K\|_1 + E \|h_{K^c}\|_1$$

$$\leq 2E \|h_K\|_1 \leq 2\sqrt{L_r} E \|h_K\|_2$$

$$\leq \frac{8\sqrt{L_r} \rho}{\beta} \left(\frac{S_w}{\sqrt{N}} \|a\|_\infty + \tilde{C}_1 (1 + P(\nu)) \|b\|_\infty E \|h\|_2 \right). \quad (32)$$

$$E \|h\|_2 \leq \frac{8\sqrt{L_r} \rho \|a\|_\infty}{\beta - 8\sqrt{L_r} \rho \tilde{C}_1 (1 + P(\nu)) \|b\|_\infty} \frac{S_w}{\sqrt{N}}. \quad (33)$$

Using (20) and (21) we get

$$E \|h\|_2 \leq \frac{72\sqrt{L_r} \rho \gamma_2}{9\beta \gamma_0 \gamma_2 - D_1 \nu^{-2} + D_2 \nu^{-4}} \frac{S_w}{\sqrt{N}}, \quad (34)$$

$$D_1 = 3\pi^2 (\beta \gamma_0 \tilde{C}_2 + 2\beta \gamma_2 \tilde{C}_0 + 8\sqrt{L_r} \rho \tilde{C}_1^2),$$

$$D_2 = 2\beta \pi^4 \tilde{C}_2 \tilde{C}_0 - 4\pi^4 \sqrt{L_r} \rho \tilde{C}_1^2.$$

For sufficiently large ν we have

$$E \|h\|_2^2 \leq \frac{64L_r \rho^2 S_w^2}{\beta^2 \gamma_0^2 N}. \quad (35)$$

This completes the proof. \square

Appendix B

Admissible Kernels and Separation Constant

To be able to quantify the waves decay and concavity we recall two definitions from previous works [4,26]:

Definition 2.1. An **admissible** kernel g is defined by the following specifications:

1. $g \in \mathbb{R}$ is real and even.
2. **Global Property:** There exist constants $C_l > 0, l = 0, 1, 2, 3$, such that $|g^{(l)}(t)| \leq \frac{C_l}{1+t^2}$, where $g^{(l)}(t)$ denotes the l^{th} derivative of g . Namely, the kernel and its first derivatives attenuate at sufficient rate.
3. **Local Property:** There exist constants $\varepsilon, \beta > 0$ such that
 - (a) $g(t) > 0$ for all $|t| \leq \varepsilon$ and $g(\varepsilon) > g(t)$ for all $|t| \geq \varepsilon$.
 - (b) $g^{(2)}(t) < -\beta$ for all $|t| \leq \varepsilon$.

The parameters ε and β measure the kernel's flatness.

In our case, all reflected waves $g_{\sigma, n}(t)$ are to be considered as admissible kernels. The reflected waves $g_{\sigma, n}(t)$ are flat at the origin, and all reflected waves share two common parameters $\varepsilon, \beta > 0$.

Definition 2.2. A set of points $K \subset \mathbb{Z}$ obeys the minimal separation condition if for a kernel dependent separation constant $\nu > 0$, a given scaling $\sigma > 0$ and a sampling interval $T_s = 1/F_s > 0$

$$\min_{k_i, k_j \in K, i \neq j} |k_i - k_j| \geq \frac{\nu \sigma}{T_s}.$$

Two distinct spikes can be recovered separately only if the time interval between them is at least $\nu \sigma$.

Appendix C

Seismic Discontinuity Measures

Seismic discontinuity measures were developed in an effort to ease seismic data interpretation and locate geological features within large volumes of data [55,56]. In the experiments presented in Section 4 we use two measures: local structural entropy (LSE) presented in [50], and skeletonized local-fault-extraction (LFE) presented in [51].

Local Structural Entropy (LSE). LSE is a discontinuity measure on a scale from zero to one. To compute the LSE, first, we reduce the mean value of each trace. Then, we choose a relatively small 3D analysis cube of size $2L_1 \times 2L_2 \times N_t$. The analysis cube is divided into four L_1 by L_2 by N_t quadrants concatenated into column vectors $\{\mathbf{v}_i | i = 1, 2, 3, 4\}$. The LSE measure associated with a distinguished point in the analysis cube (i, j, k) is

$$\mathcal{L}_s(i, j, k) = \frac{\text{tr}\Phi}{\|\Phi\|},$$

where Φ is the correlation matrix of the analysis cube:

$$\Phi = \frac{1}{N_t L_1 L_2} \begin{pmatrix} \mathbf{v}_1^T \mathbf{v}_1 & \dots & \mathbf{v}_1^T \mathbf{v}_4 \\ \vdots & \ddots & \vdots \\ \mathbf{v}_4^T \mathbf{v}_1 & \dots & \mathbf{v}_4^T \mathbf{v}_4 \end{pmatrix}.$$

Note that the LSE can be defined to associate with a point in its center by spacing out the four quadrants one trace apart from each other, using an analysis cube of size $(2L_1 + 1) \times (2L_2 + 1) \times N_t$.

If $\mathcal{L}_s(i, j, k)$ is the LSE measure as defined, then in our case we can define,

$$a_{i,j}[k] = 1 - \mathcal{L}_s(i, j, k). \quad (36)$$

It is also possible to choose a binary measure, such that $a_{i,j}[k] \in \{0, 1\}$. For example, using LSE

$$a_{i,j}[k] = \begin{cases} 1 & \mathcal{L}_s(i, j, k) < \tau, \\ 0 & \mathcal{L}_s(i, j, k) > \tau. \end{cases} \quad (37)$$

where τ is a defined threshold.

Local Fault Extraction (LFE). Computation of the LFE measure is as follows. First, we divide the 3D seismic data to 3D data analysis volumes of size $L \times M \times P$. The analysis volume is divided into two subvolumes, which are rotated and tilted around the central analysis point $p = (i, j, k)$. We rearrange the samples in the subvolumes into column vectors $\mathbf{v}_{1,p}(\theta, \phi)$ and $\mathbf{v}_{2,p}(\theta, \phi)$. Then, we compute the normalized differential entropy (NDE) of each point p as a normalized version of the Prewitt filter:

$$\mathcal{N}_p(\theta, \phi) = \frac{\|\mathbf{v}_{1,p}(\theta, \phi) - \mathbf{v}_{2,p}(\theta, \phi)\|}{\|\mathbf{v}_{1,p}(\theta, \phi)\| + \|\mathbf{v}_{2,p}(\theta, \phi)\|},$$

where $\|\cdot\|_p$ is the ℓ_p norm. Patches of fault surfaces in a presumed direction are characterized by a local increase in the NDE. Hence, we apply contrast enhancement to each NDE volume, per postulated orientation, and set negative values to zero. To enhance fault surfaces that are approximately aligned with the analysis cube we apply a directional filter $h_p(\theta + \xi, \phi)$ to the contrast-enhanced NDE $\hat{\mathcal{N}}_p(\theta, \phi)$:

$$\mathcal{C}_p(\theta + \xi, \phi) = \sum_{p'} h_{p-p'}(\theta + \xi, \phi) \hat{\mathcal{N}}_p(\theta, \phi).$$

The summation is over a set of points p' close to the point p . We then threshold the result to produce $\tilde{\mathcal{C}}_p(\theta + \xi, \phi)$, and filter it back to yield the directional LFE

$$\mathcal{L}_p(\theta, \phi) = \sum_{p', \xi} h_{p-p'}(\theta + \xi, \phi) \tilde{\mathcal{C}}_p(\theta + \xi, \phi).$$

The LFE volume is produced by taking the maximum value of the directional LFE $\mathcal{L}_p = \max_{\theta, \phi} \mathcal{L}_p(\theta, \phi)$, and further enhanced by 3D skeletonization and 3D surface separation (see [51] for further details).

References

- [1] R. Sherif, L. Geldart, *Exploration Seismology*, second ed., Cambridge University Press., UK, 1983.
- [2] A. Berkhout, The seismic method in the search for oil and gas: current techniques and future development, *Proc. IEEE* 74 (8) (1986) 1133–1159.
- [3] A. Chaouch, J.L. Mari, 3-D Land seismic surveys: definition of geophysical parameter, *Oil & Gas Sci. Technol. Rev. IFP* 61 (5) (2006) 611–630.
- [4] T. Bendory, S.D. A. Bar-Zion, A. Feuer, Stable support recovery of stream of pulses with application to ultrasound imaging, *IEEE Trans. Signal Process.* 64 (14) (2016) 3750–3759.
- [5] T. Ulrych, Application of homomorphic deconvolution to seismology, *Geophysics* 36 (6) (1971) 650–660.
- [6] R. Wiggins, Minimum entropy deconvolution, *Geoexploration* 16 (1978) 21–35.
- [7] H.L. Taylor, S.C. Banks, J.F. McCoy, Deconvolution with the ℓ_1 norm, *Geophysics* 44 (1979) 39–52.
- [8] P.V. Riel, A.J. Berkhout, Resolution in seismic trace inversion by parameter estimation, *Geophysics* 50 (1985) 1440–1455.
- [9] T. Nguyen, J. Castagna, High resolution seismic reflectivity inversion, *J. Seism. Explor.* 19 (4) (2010) 303–320.
- [10] R. Zhang, J. Castagna, Seismic sparse-layer reflectivity inversion using basis pursuit decomposition, *Geophysics* 76 (6) (2011) 147–158.
- [11] A. Gholami, M.D. Sacchi, A fast and automatic sparse deconvolution in the presence of outliers, *IEEE Trans. Geosci. Remote Sens.* 50 (10) (2012) 4105–4116.
- [12] D. Pereg, D. Ben-Zvi, Blind deconvolution via maximum kurtosis adaptive filtering, in: *Proceedings of IEEE International Conference on the Science of Electrical Engineering (ICSEE)*, 2016, pp. 1–5.
- [13] M.Q. Pham, L. Duval, C. Chaux, J.-C. Pesquet, A primal-dual proximal algorithm for sparse template-based adaptive filtering: application to seismic multiple removal, *IEEE Trans. Signal Process.* 62 (16) (2014) 4256–4269.
- [14] A. Repetti, M.Q. Pham, L. Duva, E. Chouzenoux, J.-C. Pesquet, Euclid in taxicab: sparse blind deconvolution with smoothed ℓ_1/ℓ_2 regularization, *IEEE Signal Process. Lett.* 22 (5) (2015) 539–543.
- [15] S.S. Chen, D.L. Donoho, M.A. Saunders, Atomic decomposition by basis pursuit, *SIAM Rev.* 43 (1) (2001) 129–159.
- [16] M. Elad, *Sparse and Redundant Representations*, Springer, 2010.
- [17] D. Donoho, Compressed sensing, *IEEE Trans. Inf. Theory* 52 (4) (2006) 1289–1306.
- [18] R.J. Tibshirani, The LASSO problem and uniqueness, *Electron. J. Stat.* 7 (2013) 1456–1490.
- [19] B. Efron, T. Hastie, I. Johnstone, R. Tibshirani, Least angle regression, *Ann. Stat.* 32 (2) (2004) 407–499.
- [20] V. Duval, G. Peyré, Exact support recovery for sparse spikes deconvolution, *Found. Comput. Math.* 15 (5) (2015) 1315–1355.
- [21] D.L. Donoho, Super-resolution via sparsity constraints, *SIAM J. Math. Anal.* 23 (5) (1992) 1309–1331.
- [22] C. Dossal, S. Mallat, Sparse spike deconvolution with minimum scale, in: *Proceedings of the SPARS*, 2005, pp. 123–126.
- [23] C. Fernandez-Granda, Support detection in super-resolution, in: *Proceedings of the SampTA*, 2013, pp. 145–148.
- [24] E.J. Candès, C. Fernandez-Granda, Super-resolution from noisy data, *J. Fourier Anal. Appl.* 19 (6) (2013) 1229–1254.
- [25] E.J. Candès, C. Fernandez-Granda, Towards a mathematical theory of super-resolution, *Commun. Pure Appl. Math.* 67 (6) (2013) 906–956.
- [26] T. Bendory, S. Dekel, A. Feuer, Robust recovery of stream of pulses using convex optimization, *J. Math. Anal. Appl.* 442 (2) (2016) 511–536.
- [27] J. Idier, Y. Goussard, Multichannel seismic deconvolution, *IEEE Trans. Geosci. Remote Sens.* 31 (5) (1993) 961–979.
- [28] J. Mendel, J. Kormylo, F. Aminzadeh, J. Lee, F. Habibi-Ashrafi, A novel approach to seismic signal processing and modeling, *Geophysics* 46 (1981) 1398–1414.
- [29] J. Kormylo, J. Mendel, Maximum likelihood detection and estimation of bernoulli-gaussian processes, *IEEE Trans. Inf. Theory* 28 (2) (1982) 482–488.
- [30] K. Kaarensen, T. Taxt, Multichannel blind deconvolution of seismic signals, *Geophysics* 63 (6) (1998) 2093–2107.
- [31] A. Heimer, I. Cohen, A. Vassiliou, Dynamic programming for multichannel blind seismic deconvolution, in: *Proceedings of the Society of Exploration Geophysicist International Conference, Exposition and Seventy-Seventh Annual Meeting*, San Antonio, 2007, pp. 1845–1849.
- [32] A. Heimer, I. Cohen, Multichannel seismic deconvolution using Markov-Bernoulli random field modeling, *IEEE Trans. Geosci. Remote Sens.* 47 (7) (2009) 2047–2058.
- [33] A. Heimer, I. Cohen, Multichannel blind seismic deconvolution using dynamic programming, *Signal Process.* 88 (4) (2008) 1839–1851.
- [34] I. Ram, I. Cohen, S. Raz, Multichannel deconvolution of seismic signals using statistical MCMC methods, *IEEE Trans. Signal Process.* 58 (5) (2010) 2757–2769.
- [35] M. Mirel, I. Cohen, Multichannel semi-blind deconvolution of seismic signals, *Signal Process.* 135 (2017) 253–262.
- [36] A. Gholami, M.D. Sacchi, Fast 3d blind seismic deconvolution via constrained total variation and GCV, *SIAM J. Imaging Sci.* 6 (4) (2013) 2350–2369.

- [37] D. Forney, The viterbi algorithm, *Proc. IEEE* 61 (3) (1973) 268–278.
- [38] E. Kjartansson, Constant q -wave propagation and attenuation, *J. Geophys. Res.* 84 (1979) 4737–4747.
- [39] L. Gelius, Inverse q filtering, a spectral balancing technique, *Geophys. Prospect.* 35 (1987) 656–667.
- [40] D. Hale, An inverse Q filter, Stanford Exploration Project Report (26) (1981) 231–243.
- [41] Y. Wang, *Seismic Inverse Q-Filtering*, Blackwell Pub, 2008.
- [42] G. Margrave, M.P. Lamoureux, D. Henley, Gabor deconvolution: estimating reflectivity by nonstationary deconvolution of seismic data, *Geophysics* 76 (3) (2011) W15–W30.
- [43] X. Chai, S. Wang, S. Yuan, J. Zhao, L. Sun, X. Wei, Sparse reflectivity inversion for nonstationary seismic data, *Geophysics* 79 (3) (2014) V93–V105.
- [44] A. Rosa, T.J. Ulrych, Processing via spectral modeling, *Geophysics* 56 (8) (1991) 1244–1251.
- [45] F. Li, S. Wang, X. Chen, G. Liu, Q. Zheng, A novel nonstationary deconvolution method based on spectral modeling and variable-step sampling hyperbolic smoothing, *J. Appl. Geophys.* 103 (2014) 132–139.
- [46] D. Pereg, I. Cohen, Seismic signal recovery based on earth Q model, *Signal Process.* 137 (2017) 373–386, doi:10.1016/j.sigpro.2017.02.016.
- [47] N. Ricker, The form and nature of seismic waves and the structure of seismogram, *Geophysics* 5 (4) (1940) 348–366.
- [48] Y. Wang, Frequencies of the ricker wavelet, *Geophysics* 80 (2) (2015) A31–A37.
- [49] Y. Wang, A stable and efficient approach of inverse Q filtering, *Geophysics* 67 (2) (2002) 657–663.
- [50] I. Cohen, R. Coifman, Local discontinuity measures for 3d seismic data, *Geophysics* 67 (6) (2002) 1933–1945.
- [51] I. Cohen, N. Coult, A.A. Vassiliou, Detection and extraction of fault surfaces in 3D seismic data, *Geophysics* 71 (4) (2006) P21–P27.
- [52] D. Pereg, I. Cohen, A.A. Vassiliou, Multichannel sparse spike inversion, *J. Geophys. Eng.* 14 (5) (2017) 1290.
- [53] M. Grant, S. Boyd, *CVX: Matlab software for disciplined convex programming*, 2014, (version 2.1).
- [54] C. Zhang, T. Ulrych, Estimation of quality factors from CMP record, *Geophysics* 67 (5) (2002) 1542–1547.
- [55] M.S. Bahorich, S.L. Farmer, *3D Seismic Discontinuity for Faults and Stratigraphic Features: The Coherence Cube*, 14, the Leading Edge, 1995, pp. 1053–1058. 10.
- [56] A. Gersztenkorn, K.J. Marfurt, Eigenstructure-based coherence computations as an aid to 3-D structural and stratigraphic mapping, *Geophysics* 64 (5) (1999) 1468–1479.